Journal of Solid State Chemistry **155,** 96–104 (2000)
doi:10.1006/jssc.2000.8904, available online at http://www.idealibrary.com on IDEAL®

Properties of the $n = 3$ Ruddlesden–Popper Phases $Sr_4Mn_{3-x}Fe_xO_{10-\delta}$ ($x = 1$, 1.5, 2)

Ian D. Fawcett, Gabriel M. Veith, and Martha Greenblatt[1]

Department of Chemistry, Rutgers, State University of New Jersey Piscataway, New Jersey 08854

Mark Croft

Department of Physics and Astronomy, Rutgers, State University of New Jersey, Piscataway, New Jersey 08854

and

Israel Nowik

Racah Institute of Physics, Hebrew University, Jerusalem, 91904 Israel

Received May 30, 2000; in revised form July 25, 2000; accepted July 28, 2000

DEDICATED TO PROFESSOR J. M. HONIG

We have prepared a series of Fe-substituted $Sr_4Mn_{3-x}Fe_xO_{10-\delta}$ strontium manganates with $x = 1$, 3/2, and 2. These compounds adopt the $n = 3$ Ruddlesden–Popper structure ($I4/mmm$), unlike the parent compound $Sr_4Mn_3O_{10}$, which contains a network of face-sharing MnO_6 octahedra, with the larger Fe ion preferentially occupying the Mn/Fe (1) middle layer of the corner-sharing trioctahedra slabs. We have investigated their physical properties with X-ray diffraction, X-ray absorption near edge spectroscopy, Mössbauer spectroscopy, variable temperature resistivity, and magnetic susceptibility. In addition, for the $x = 2$ compound we preformed room temperature neutron diffraction experiments. These compounds need to be formed at high temperatures; as a consequence they are oxygen deficient and contain some Fe^{3+}. They are insulators and exhibit spin-glass-like transitions at low temperature. © 2000 Academic Press

INTRODUCTION

Transition metal oxides have been studied extensively due to their fascinating structural, electronic, and magnetic behavior. In recent years, research has focused on the manganates, $Ln_{1-x}A_xMnO_3$ (Ln = rare earth ion, A = alkali or alkaline earth metal ion) (1), which contain mixed-valence manganese in a perovskite structure. The magnetotransport properties of the manganates, such as colossal magnetoresistance (CMR), have been explained in terms of the double exchange theory (2), whereby ferromagnetic interactions between Mn^{3+} ($3d^4$)/Mn^{4+} ($3d^3$) are mediated by the conduction electrons.

[1] To whom correspondence should be addressed.

Recently, other $3d^3/3d^4$ systems have been studied to investigate whether double exchange and the properties observed in the CMR manganates can be replicated. Gundakaram *et al.* (3) synthesized the phase, $LaMn_{1-x}Cr_xO_3$, containing Mn^{3+} ($3d^4$) and Cr^{3+} ($3d^3$). Ferromagnetic coupling was preserved but the compounds were insulators and CMR was not observed. Battle *et al.* (4) synthesized the $n = 3$ Ruddlesden–Popper (RP) (5) phases, $Ca_4Mn_2FeO_{9.75}$ and $Sr_4Mn_2FeO_{9.80}$, containing Mn^{4+} ($3d^3$) and Fe^{4+} ($3d^4$). Both compounds were shown to be insulators that ordered antiferromagnetically at 75 K (Ca) and 90 K (Sr) with a spin-glass transition at $\sim$11 K. d^3/d^4 coupling was achieved but electron localization made it a superexchange rather than a double-exchange interaction. This study also showed that $Sr_4Mn_2FeO_{9.80}$ adopted the $n = 3$ RP structure in contrast to the "parent" compound $Sr_4Mn_3O_{10}$, which crystallizes in a structure containing triple groups of face-shared MnO_6 octahedra interconnected by common corners into a two-dimensional framework perpendicular to the [010] direction (6). The $n = 3$ RP structure, Fig. 1, can be thought of as three layers of MO_6 octahedra along the c axis separated by an insulating rock-salt layer. In the $n = 3$ RP phases the outer MO_6 octahedra only have 5 MO_6 octahedra surrounding them rather than 6 MO_6 octahedra commonly seen in $n = \infty$ phases and the inner layer of the $n = 3$ phase. This octahedra configuration offers unique opportunities to adjust the magnetic interactions and electrical conductivity to tailor the physical properties of compounds. The replacement of $\frac{1}{3}$ of the Mn ions by Fe stabilizes the $n = 3$ RP structure possibly due to size effects ($r(Mn^{4+}) = 0.67$ Å, $r(Fe^{4+}) = 0.725$ Å) (7).

0022-4596/00 $35.00

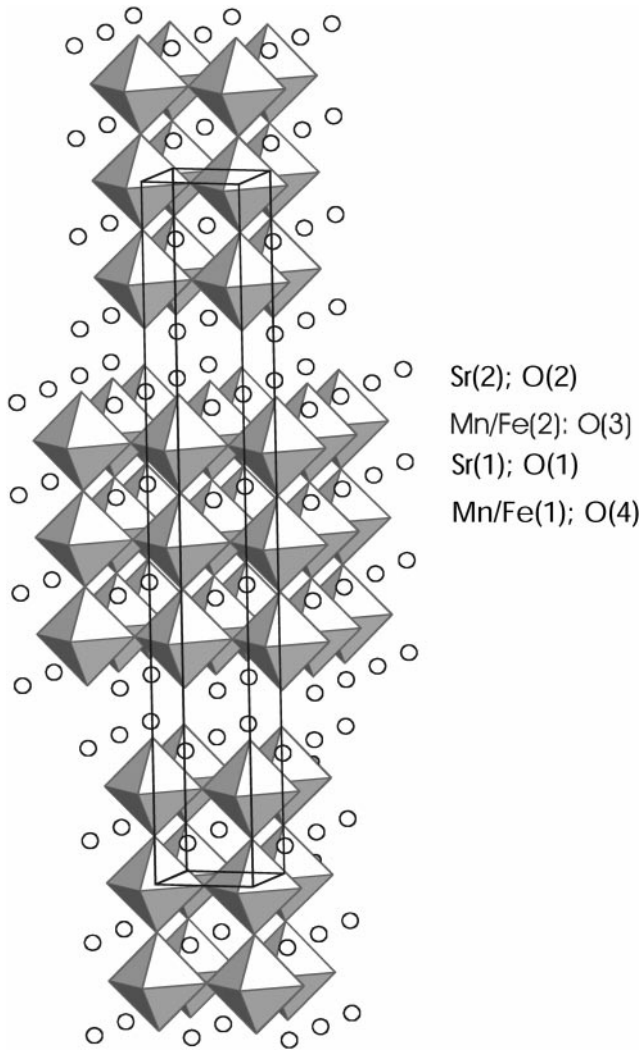

FIG. 1. The $n = 3$ Ruddlesden–Popper Structure. The shaded octahedra are Fe/Mn–O_6 and the circles are Sr atoms.

This paper describes the magnetic and electronic properties of the phases $Sr_4Mn_{3-x}Fe_xO_{10-\delta}$ ($x = 1$, 1.5, 2) containing a $3d^3/3d^4$ system. The structure of $Sr_4MnFe_2O_{10-\delta}$ is examined in greater detail using powder neutron diffraction to study cation and anion disorder.

EXPERIMENTAL

Samples were prepared by mixing stoichiometric quantities of $SrCO_3$, Fe_2O_3, and MnO_2. The reaction mixture was pressed into pellets and heated in air at 800°C for 1 day, 1000°C for 1 day, 1200°C for 1 day, and 1300°C for 7 days. The mixture was reground frequently, and the reaction was monitored by powder X-ray diffraction (PXD). PXD data was collected at room temperature with a Scintag PAD V diffractometer employing Cu$K\alpha$ radiation over the range $20^\circ \leq 2\theta \leq 120^\circ$, with a step size of 0.02°. In order to derive accurate lattice parameters, silicon was added as an internal standard.

Time-of-flight neutron data were collected for the $x = 2$ sample at the Intense Pulsed Neutron Source (IPNS), Argonne National Laboratory (ANL). The sample was sealed in a cylindrical vanadium can, and diffraction experiments were carried out on the General Purpose Powder Diffractometer (GPPD). Data were collected at room temperature covering the range $0.70 \leq d/\text{Å} \leq 2.89$. Rietveld refinement of the data was performed using the program GSAS (8).

Oxygen content of the samples was determined by iodometric titration employing amperometric dead-stop end-point detection using the technique described by Licci *et al.* (9).

X-ray absorption spectroscopy (XAS). The Mn and Fe K-edge XAS measurements were performed on beam lines X-19A and X-18B at the Brookhaven National Synchrotron Light Source using a double-crystal Si (311) monochromator. Electron yield, fluorescence mode, and transmission mode measurements were made and checked for consistency. The relative energies between various spectra were established by careful comparison of the standard spectra. Particular care was taken to use an identical standard sample, which was maintained in a constant position to accurately calibrate the chemical shift results. In general, the relative accuracy of the energy is about $\pm$ 0.05eV. All spectra were normalized to unity step in the absorption coefficient from well below to well above the edge.

Mössbauer studies. These studies were performed using a ^{57}Co:Rh source (50 mCi) and a conventional constant acceleration Mössbauer drive. Spectra of the three samples were collected at 4.2 and 200 K. The spectra were analyzed and least-square fitted by a computer program that allowed a Gaussian distribution of magnetic hyperfine fields in the 4.2-K spectra and a quadruple interaction distribution in the 200-K spectra.

Magnetic susceptibilities. Magnet susceptibilities of the samples were obtained using a Quantum Design SQUID magnetometer over the temperature range 5–300 K in an applied field of 1000 G. Data were collected after cooling in zero field (ZFC) and in an applied field (FC).

Resistivity. These measurements were made using a standard four-probe method over a temperature range of 120–300 K. Gold wire contacts were attached to the sintered polycrystalline samples with silver paint. The estimated uncertainty in the room-temperature resistivity (ρ_{RT}) is $\sim$20%.

RESULTS AND DISCUSSIONS

The $Sr_4Mn_{3-x}Fe_xO_{10-\delta}$ phases with $x = 1$, 1.5, 2 have been successfully synthesized. The powder X-ray diffraction

TABLE 1
Physical Properties of $Sr_4Mn_{3-x}Fe_xO_{10-\delta}$

Compound	$Sr_4Mn_2FeO_{9.72}$	$Sr_4Mn_{1.5}Fe_{1.5}O_{9.68}$	$Sr_4MnFe_2O_{9.51}$
a (Å)	3.83424(6)	3.84223(4)	3.8506(9)
c (Å)	27.8023(9)	27.8723(5)	27.964(1)
T_g (K)	10(5)	25(5)	25(5)
T_N (K)	90(5)	—	—
θ (K)	−32(3)	−8(3)	−7(5)
C (emu K mol^{-1})	7.60(4) (150–300 K)	8.37(5) (100–300 K)	8.53(6) (100–300 K)
C_{theo}(emu K mol^{-1})	7.43	8.34	9.25
μ_{eff} (μ_B)	7.79	8.18	8.26
μ_{theo} (μ_B)	7.71	8.16	8.60
ρ_{RT} (Ω-cm)	1.1×10^3	2.4×10^2	28
E_a (eV) [T_{range} (K)]	0.22 eV (300–237)	0.22 eV (300–260)	0.19 eV (290–240)

Note. T_g is the spin-glass transition temperature.

patterns were consistent with the formation of $n = 3$ RP phases. The lattice parameters, listed in Table 1, show a linear increase with x, as would be expected from the substitution of larger Fe^{3+} ($r_{eff} = 0.785$ Å) and Fe^{4+} ($r_{eff} = 0.72$ Å) for the smaller Mn^{4+} ($r_{eff} = 0.670$ Å) (7).

Iodometric titrations show that the samples are all oxygen deficient, the deficiency increasing with x, due to the difficulty of synthesizing Fe^{4+}-containing compounds in air, Table 1. Typically, only mixed Fe^{4+}/Fe^{3+} phases can be obtained under ambient oxygen pressure. Further analysis of the transition metal oxidation states was performed using XAS, as described below.

Refinements of the room temperature neutron diffraction data for $Sr_4MnFe_2O_{10-\delta}$ were performed in the space group $I4/mmm$ using the parameters for $Sr_4Mn_2FeO_{9.80}$ as a starting model (4). The distribution of transition metals over the two available sites was varied, constraining the Mn:Fe ratio to 2:1, and the oxygen occupancy was refined. Since the occupancy of O(2) and O(3) (Fig. 1) refined to a value close to unity they were fixed at one in the final refinement. The structural parameters are listed in Table 2, and the derived bond lengths and bond angles are presented in Table 3. The observed and calculated diffraction patterns are shown in Fig. 2. The refinement suggests that the majority of anion vacancies occur on sites O(1) and O(4), which are coordinated to the cation at the center of the perovskite trilayers. Mn and Fe preferentially occupy the outer and central layers, respectively. The Mn/Fe(2)–O(1) bond distances are longer than the Mn/Fe(2)–O(2) bond lengths. These results can be rationalized using similar arguments as those of Battle *et al.* (4). If we reason that the larger Fe^{3+} is located in the central layer and the smaller Mn^{4+} and Fe^{4+} ions are located in the outer layer, the higher oxidation state metals in the outer layer pull the axial oxygen O(2) closer. Indeed there is a decrease in the bond length between Mn/Fe(2) and O(2) from those reported by Battle *et al.* (4), 1.901 vs 1.919 Å, and an elongation of the Mn/Fe(2)–O(1) bond, 2.076 vs 1.997 Å (4), due to an increase in oxygen vacancies and a larger concentration of higher valent ions in the Mn/Fe(2) site in our compound.

The use of neutrons to study order/disorder in these compounds is advantageous due to the different scattering lengths of the Mn and Fe for neutrons versus X-rays. The neutron data for the $x = 2$ phase would be expected to have superlattice lines, if, for example, the 2a site (middle octahedra in the MnO layer) had 100% Fe occupancy. The absence of any superlattice reflections rules out ordering of the cations. Thus the Mn and Fe ions appear to be distributed randomly in all the layers, but with a majority of Fe ions (15.3/84.7%) located within the middle Mn/Fe(1) layer (Fig. 1). It is interesting to note that the substitution of the larger Fe into the middle layer of the $n = 3$ phase seems to stabilize the structure, allowing it to form the Ruddlesden–Popper phase rather than the face-sharing octahedral structure seen in the $Sr_4Mn_3O_{10}$ compound. Hexaganol $Sr_4Mn_3O_{10}$ could only be synthesized by doping a small amount (1%) of platinum impurity into the structure (6).

TABLE 2
Structural Parameters of $Sr_4MnFe_2O_{10-\delta}$ at Room Temperature

Atom	Site	Occupancy	x	y	z	U_{iso} (Å^2)
Sr(1)	4e	1	0	0	0.5713(3)	0.006(1)
Sr(2)	4e	1	0	0	0.70209(2)	−0.003(1)
Mn/Fe(1)	2a	0.153/0.847(11)	0	0	0	0.003(2)
Mn/Fe(2)	4e	0.423/0.577(6)	0	0	0.1422(3)	−0.003(2)
O(1)	4e	0.904(15)	0	0	0.0679(3)	0.020(3)
O(2)	4e	1	0	0.5	0.2102(2)	0.001(2)
O(3)	8g	1	0	0.5	0.6371(2)	0.003(1)
O(4)	4c	0.851(15)	0	0.5	0.5	0.011(3)

Note. Space group $I4/mmm$; $a = 3.8509(2)$ Å, $c = 27.964(1)$ Å, $V = 414.70(5)$ Å^3. $R_{wp} = 7.90\%$, $R_p = 5.57\%$, $\chi^2_{red} = 3.457$ for 39 variables.

TABLE 3
Bond Lengths (Å) and Bond Angles (°) in $Sr_4MnFe_2O_{10-\delta}$ at Room Temperature

Sr(1)–O(1) × 4	2.7246(8)
Sr(1)–O(3) × 4	2.665(6)
Sr(1)–O(4) × 4	2.770(4)
Sr(2)–O(2) × 1	2.454(6)
Sr(2)–O(2) × 4	2.7322(5)
Sr(2)–O(3) × 4	2.647(5)
Mn/Fe(1)–O(1) × 2	1.899(8)
Mn/Fe(1)–O(4) × 4	1.9254(5)
Mn/Fe(2)–O(1) × 1	2.076(9)
Mn/Fe(2)–O(2) × 1	1.901(6)
Mn/Fe(2)–O(3) × 4	1.9306(6)
Mn/Fe(1)–O(4)–Mn/Fe(1)	180
Mn/Fe(2)–O(3)–Mn/Fe(2)	171.5(6)
Mn/Fe(1)–O(1)–Mn/Fe(2)	179.97(2)

The larger Pt^{4+} ion ($r_{eff} = 0.765$ Å), like Fe^{4+} in the analogous RP phases, is located in the middle of the three face-sharing MnO_6 octahedra in the $Sr_4Mn_3O_{10}$ structure, apparently stabilizing the phase (6). While several groups have attempted to synthesize $Sr_4Mn_3O_{10}$ in the past (6, 10), only very recently Flores *et al.* have been able to prepare pure $Sr_4Mn_3O_{10}$ without incorporating a larger cation in the *B* site (11). However, we have preliminary evidence that the preferential ordering of Fe within the middle layer of the $n = 3$ RP, $Sr_4Mn_{3-x}Fe_xO_{10-\delta}$ stabilizes the structure and is essential for the formation of the RP phase. It is noteworthy that the other end member of the series, $Sr_4Fe_3O_{10}$, has never been synthesized either. While we and others (12) have attempted to form the $n = 3$ strontium ferrate, the product is always a mixture of $SrFeO_3$ perovskite and the $n = 2$, $Sr_3Fe_2O_7$ compound. Thus the mixture of Mn and Fe at the perovskite *B* site seems to be essential to stabilize the $n = 3$ RP phase, $Sr_4Fe_3O_{10-\delta}$.

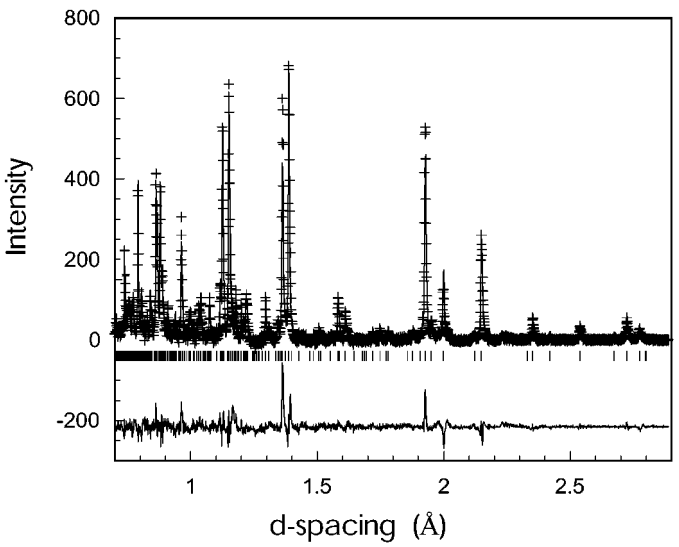

FIG. 2. Observed (+), calculated (solid line), and allowed reflections (tic) neutron diffraction data for $Sr_4MnFe_2O_{9.51}$. Difference plot is at the bottom.

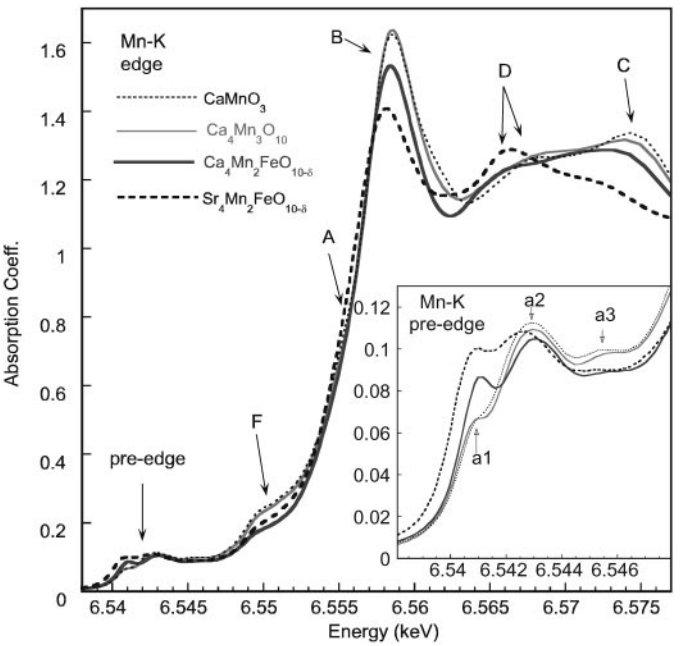

FIG. 3. The Mn–K main edges of $CaMnO_3$, $Ca_4Mn_3O_{10-\delta}$, and $A_4Mn_2FeO_{10-\delta}$ (A = Ca and Sr). The spectral feature labeling is provided to clarify the discussion in the text. (Inset) The Mn–K preedges of $CaMnO_3$, $Ca_4Mn_3O_{10-\delta}$, and $A_4Mn_2FeO_{10-\delta}$ (A = Ca and Sr); coordinate axis labels are the same as those of the main figure.

It is well documented that these RP phases are susceptible to a variety of defects (4,13), such as stacking faults. Instead of a well-ordered system with 1, 2, or 3 perovskite layers (i.e., for the $n = 1$, 2, and 3 phases respectively) separated by the AO rock-salt layer, there are often stacking faults with higher order members incorporated into the structure. These stacking faults can only be elucidated with high-resolution electron microscopy (HREM); hence it is impossible to rule out the presence of higher (or lower) member slabs of intergrowth in the compounds studied here.

XAS. Figure 3 compares the Mn–K main and pre-edges of the formally Mn^{4+} standards $CaMnO_3$ (113) and $Ca_4Mn_3O_{10}$ (4310) with the Fe-substituted $A_4Mn_2FeO_{10-\delta}$ (A = Ca and Sr) compounds. The main edges of the Ca-113 and -4310 compounds are very similar. The spectrum of the Fe-substituted Ca-4310 material manifests several changes: the B peak has shifted slightly to lower energy and has become less intense; there has been a loss of intensity in the C feature region relative to the D region of the spectrum; the foot-F feature has lost intensity; and there are strong pre-edge feature changes (discussed below). The downward shift in energy of the B feature has been correlated with a

decreasing average Mn valence in previous Mn–perovskite-based compound studies (14). In a more secondary way the loss of intensity in the D feature has also been correlated with a decreased Mn valence in such systems (15). The small magnitude of the B feature shift indicates that any Mn valence change is quite small.

In the $Sr_4Mn_2FeO_{10-\delta}$ spectrum (see Fig. 3) the B feature has been shifted to lower energy, decreased in amplitude, and broadened with respect to that of $Ca_4Mn_2FeO_{10-\delta}$. Indeed the B broadening partially takes the form of additional intensity on the leading edge near the position labeled A. The fine structure in the D–C regions of the Sr compound spectrum are strongly changed presumably due to the very different photoelectron backscattering of Sr relative to Ca. The downward shift of the B feature is not likely to be due to a decrease of the Mn valence in the Sr-based (versus the Ca) material as a higher valence of Mn is expected for the more basic Sr cation.

The preedge features of these Mn spectra (see Inset of Fig. 3) are associated with transitions involving d final states through either quadrupole or dipole (through d–p hybridization) transitions. Again the Ca-based materials will be discussed first. In the preedge spectra of the Ca-113 and -4310 compounds (Fig. 3), three distinctive features (a1, a2, and a3) of the Mn^{4+} state are identifiable. Of the preedge changes between the 113 and the 4310 spectra the pronounced a1 feature enhancement is the most noticeable. Electronic structure calculations (16) and optical absorption (17)-based electronic state distributions both clearly support the majority-spin e_g-states assignment for the a1 feature (the lowest lying of the unfilled $3d$ states in Mn^{4+}). Within this assignment two effects could contribute to this a1-feature enhancement in the 4310 spectrum: the loss of centrosymmetry about the Mn sites (particularly at the perovskite-layer/CaO -layer boundary) in the apical direction could enhance d–p mixing, and with it, strengthen dipole allowed transitions to e_g states aligned along the apical direction. The e_g states aligned in this apical direction could also be more localized and therefore have a larger transition matrix element.

It is important to note that upon Fe substitution into the Ca-4310 material, the a1 feature is *dramatically* enhanced. The $Sr_4Mn_2FeO_{10-\delta}$ compound shows an even stronger enhancement of the a1 feature. Indeed Fe substitution into 113 and 327 manganites has consistently been shown to induce similar (albeit somewhat smaller) a1-feature enhancements (18, 19). Again based on the above a1 assignment, this would imply a Fe substitution-induced enhancement of transitions into the majority-spin e_g final states. It has been proposed that this effect is related to the localization of the Mn e_g orbitals upon Fe substitution (17, 20–22). Specifically the energy mismatch between the Fe and Mn d orbitals leads to the removal of Mn-intersite hopping paths (channels) with Fe substitution and therefore to increased Mn localization (22). Indeed XAS results in our lab have confirmed this Fe-modification trend in the $Sr_3Mn_{2-x}Fe_xO_{7-\delta}$ and $SrMn_{1-x}Fe_xO_{3-\delta}$ Ruddlesden–Popper phases of the manganates (18, 19). Further, it should be pointed out that extension of the same argument to the Fe sites would imply an analogous Mn-substitution-induced localization of the Fe d states. The Mössbauer results unambiguously favor such localization. Namely, similar to $SrFeO_{3-\delta}$, which exhibits mixed valent Fe^{4+}/Fe^{3+}, our Mn-substituted materials all exhibit a "disproportionated" localization of the Fe d states with differing d counts at differing sites (18). Thus the mutual localization of the Mn and Fe d states (near the Fermi energy) in the mixed (Mn, Fe) materials is supported.

The compositional dependence of the Mn–K main and preedges in the $Sr_4Mn_{3-x}Fe_xO_{10-\delta}$ compound series is illustrated in Fig. 4. The central observation regarding Fig. 4 is that the structure and chemical shift of the edge remain essentially constant as a function of Fe substitution. In contrast, in the preedge spectra of Fig. 4 (Inset), the Fe substitution systematically enhances and sharpens the a1 feature while degrading the a2 feature. This result is consistent with the argument for Fe-induced localization of the Mn e_g orbitals mentioned above.

The $Sr_4Mn_{3-x}Fe_xO_{10-\delta}$ ($x = 1.0$, 1.5, and 2.0) Fe–K main edge spectra show only modest changes with increasing Fe content, Fig. 5. There is some sharpening of the main

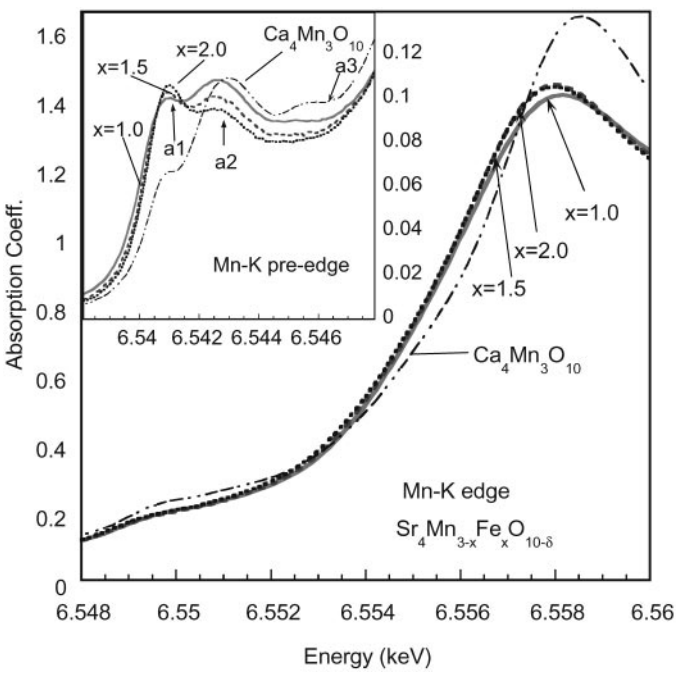

FIG. 4. The Mn–K main edges of $Ca_4Mn_3O_{10-\delta}$, and $Sr_4Mn_{3-x}Fe_xO_{10-\delta}$ ($x = 1.0$, 1.5, and 2.0). (Inset) The Mn–K preedges of $Ca_4Mn_3O_{10-\delta}$, and $Sr_4Mn_{3-x}Fe_xO_{10-\delta}$ ($x = 1.0$, 1.5, and 2.0); coordinate axis labels are the same as those of the main figure.

peak with increasing Fe content; however, the chemical shift at all x values is consistent with that of to $SrFeO_{3-\delta}$. Thus the formal Fe valence appears to remain close to Fe^{4+} in these $Sr_4Mn_{3-x}Fe_xO_{10-\delta}$ materials. It must be emphasized however that previous work within our group has shown Fe–K edge XAS to be rather insensitive to partial Fe-valence disproportionation (18, 19). In general the Fe–K main edges have a less well-defined peak and more intensity in features both below and above the main peak as compared to the Mn–K spectra discussed above. This presumably reflects the greater importance of a configurational admixture for Fe in these materials relative to the Mn.

The Fe–K preedge spectra of $Sr_4Mn_{3-x}Fe_xO_{10-\delta}$ ($x =$ 1.0, 1.5, and 2.0) manifest a rather strong variation with increasing Fe content. The $x = 2$ spectrum exhibits a peak at a position, identified as b1 in Fig. 5 (Inset), that is close to the sharp peak in $SrFeO_{3-\delta}$. With increasing Fe content this b1 feature appears to remain, however a second higher-energy feature, at the position labeled b2, gains intensity.

Association of the Fe–K preedge features with specific d states, as in the Mn case, is not possible with the spectral resolution of the present data. However, the rather distinct change from a sharp single feature for the $x = 2.0$ compound to distinctly bimodal features for the Mn-substituted compounds are supportive of the Fe-site localization into two sites.

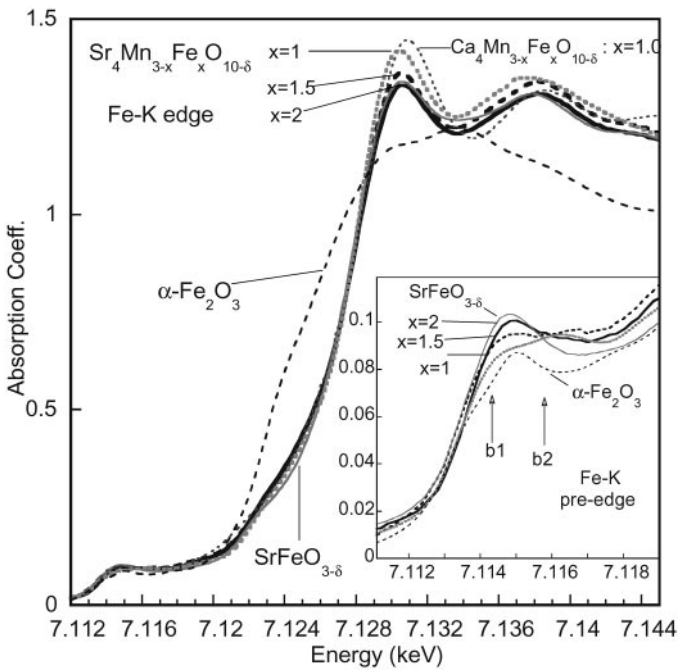

FIG. 5. The Fe–K main edges of the $Sr_4Mn_{3-x}Fe_xO_{10-\delta}$ ($x = 1.0$, 1.5, and 2.0) compounds along with those of the α-Fe_2O_3 and $SrFeO_{3-\delta}$. (Inset) The Fe–K preedges of the $Sr_4Mn_{3-x}Fe_xO_{10-\delta}$ ($x = 1.0$, 1.5, and 2.0) compounds along with those of α-Fe_2O_3 and $SrFeO_{3-\delta}$ coordinate axis labels are the same as those of the main figure.

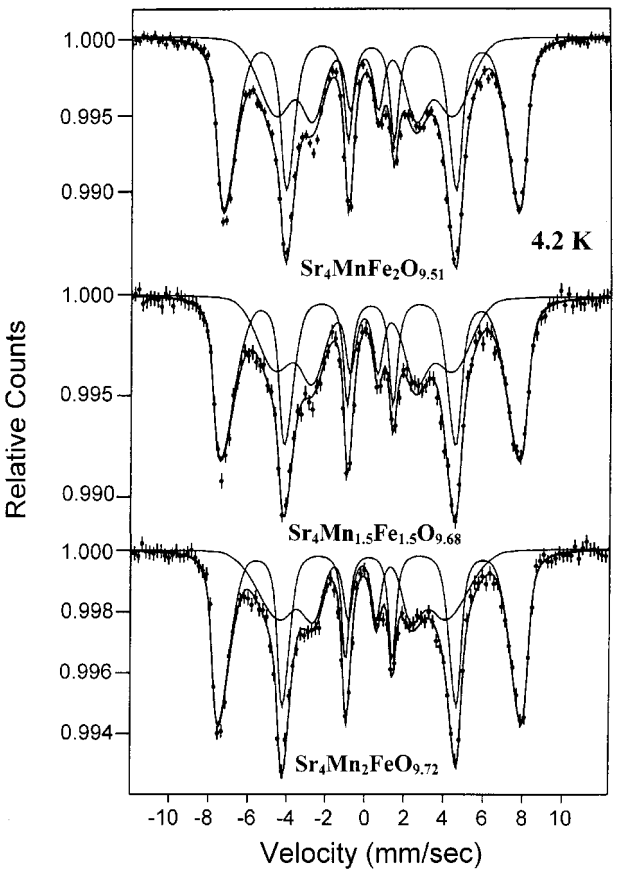

FIG. 6. Mössbauer spectra of ^{57}Fe in $Sr_4Mn_{3-x}Fe_xO_{10-\delta}$ at 4.2 K.

The Mössbauer spectra of the three samples are given in Fig. 6 (4.2 K) and Fig. 7 (200 K). The spectra were analyzed in terms of two inequivalent iron species corresponding to two different iron valence states, in terms of their isomer shift (IS) values, quadrupole splitting (ΔE_Q), and magnetic hyperfine field (B_{hf}), all of which are given in Table 4. In principle, the spectra had to be analyzed in terms of four iron species (two valences in two inequivalent crystallographic sites, 2a and 4e). However since the hyperfine parameters have a wide distribution (in the actual analysis they were assumed to have a Gaussian distribution), such an analysis is impossible. The fact that the spectra could be analyzed assuming only two iron species indicates that Fe ions of the same valence located in the two crystallographic sites have similar hyperfine interaction parameters. An alternative possibility is that the Fe ions prefer to occupy a single site (2a).

The spectra shown in Figs. 6 and 7 look very similar to the spectra previously observed for the $n = 2$ and $n = \infty$ Ruddlesden–Popper systems (18, 19). Also the hyperfine interaction parameters are similar. However there is one major difference, in contrast to the measured relative spectral

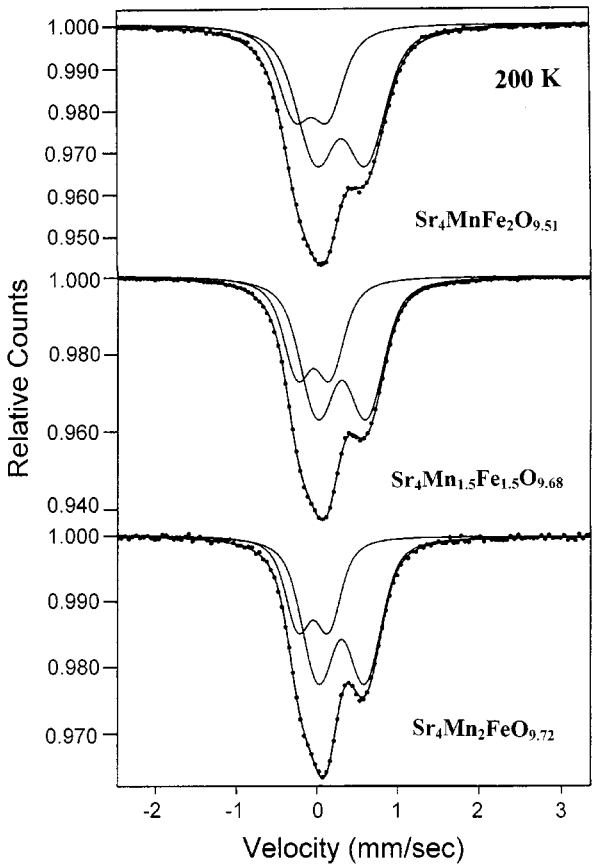

FIG. 7. Mössbauer spectra of ^{57}Fe in $Sr_4Mn_{3-x}Fe_xO_{10-\delta}$ at 200 K.

areas in the other systems. In the present case, the relative amount of the two iron species (Area in Table 4) is temperature independent, and surprisingly enough also Fe concentration (x) independent. Using the IS values of $LaFe^{3+}O_3$ (0.47) and $La_2LiFe^{5+}O_6$ (-0.43), the estimate of Fe valences of the two species observed here are $\sim +3.2$ (IS ≈ 0.35–0.4) and $+4.3$ (IS ≈ -0.2–0.06) (18, 19). This behavior is consistent with the observations in the other Ruddlesden–Popper systems, in which the Fe ions "disproportionate" into two sites, each with a fractional valence (18, 19). Here the term "disproportionation" refers to a generalization of $2Fe^{4+} \rightarrow Fe^{3+} + Fe^{5+}$ to $2Fe^{4+} \rightarrow Fe^{3+\varepsilon} + Fe^{4+\delta}$. Indeed the Fe valence state of the IS ~ -0.2 to 0.06 Mössbauer sites must fall in the range $+4.5$ or below to be reconciled with the estimated oxygen content.

The temperature dependence of the molar magnetic susceptibility is shown in Fig. 8. A local maximum is observed at 90 K when $x = 1$, which is in good agreement with data reported for $Sr_4Mn_2FeO_{9.80}$ (4). The ZFC and FC susceptibilities diverge at lower temperatures, with a maximum in the ZFC curve at 10 K for $x = 1$, and 25 K for $x = 1.5$ and 2. Fitting the high-temperature region to a Curie–Weiss law

TABLE 4
Mössbauer Parameters for $Sr_4Mn_{3-x}Fe_xO_{10-\delta}$

	$x = 1$, $\delta = 0.28$		$x = 1.5$, $\delta = 0.32$		$x = 2$, $\delta = 0.49$	
Temp(K)	4.2	200	4.2	200	4.2	200
Site 1						
IS	0.40	0.35	0.41	0.35	0.41	0.35
ΔE_Q	0.0	0.58	0.0	0.60	0.0	0.62
B_{hf}	494	0.0	491	0.0	483	0.0
Area (%)	58	61	57	58	58	60
Site 2						
IS	0.06	0.00	0.09	0.01	0.06	-0.02
ΔE_Q	0.0	0.38	0.0	0.41	0.0	0.41
B_{hf}	261	0.0	283	0.0	286	0.0
Area (%)	42	39	43	42	42	40
ΔIS	0.34	0.35	0.32	0.34	0.35	0.37
ΔB	233	0.0	208	0.0	197	0.0

Note. The IS ($\pm$ 0.02, relative to iron metal) and ΔE_Q ($\pm$ 0.02) have units of mm s^{-1}; B_{hf} ($\pm$ 10) has units of kOe. The error on the relative Area is $\pm 2\%$.

gave the parameters listed in Table 1. The Weiss constants, θ, are negative indicating antiferromagnetic interactions between the disordered magnetic ions dominating in the $n = 3$ RP phases. The magnetic susceptibility of these iron-substituted strontium manganates is very similar to other mixed transition metal compounds (23). Reported neutron scattering experiments on the $x = 1$ compound indicate that there is no magnetic ordering in the inner iron-rich layer, while the magnetic ions in the outer layer interact weakly (4). Some ions do not order at all and are responsible for the spin-glass-like ordering at low temperatures (4).

The calculated Curie constants, C, and μ_{eff} for the $x = 1$ and 1.5 phases are close to the spin-only predicted values, while for the $x = 2$ sample the value is significantly lower than predicted (Table 1). Our calculated C value for the $x = 2$ material is smaller than previously reported (4). Perhaps this is due to the lower oxygen content of our sample, which would increase the Fe^{3+} content; Fe^{3+}–O–Fe^{3+} interactions are AFM (4). Thus even with a random distribution of ions, the domains of Fe^{3+}–O–Fe^{3+} with AFM interactions increase, thereby effectively lowering C (24).

Due to preparatory techniques and the necessity of high reaction temperatures and long reaction times, it is not surprising that the compounds are oxygen deficient. This oxygen deficiency leads to complicated magnetic interactions. It is difficult to draw an accurate description of the magnetic results without performing further neutron experiments on our compounds at low temperatures. We note that the randomly distributed ions introduce a large number of potential interactions including AFM Mn^{4+}–O–Mn^{4+}, and Fe^{3+}–O–Fe^{3+}, and both FM and AFM interactions between the Fe and Mn ions through the σ and π orbitals respectively. These complicated magnetic interactions can

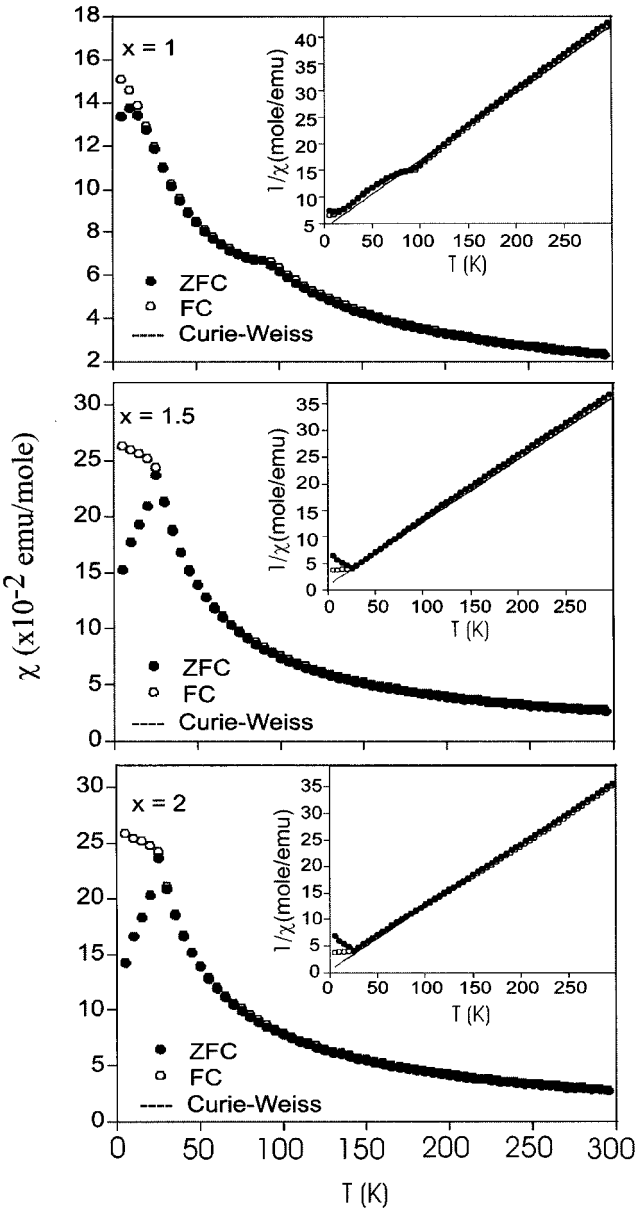

FIG. 8. Temperature-dependent magnetic susceptibility data for $Sr_4Mn_{3-x}Fe_xO_{10-\delta}$. (Inset) Inverse susceptibility vs temperature.

result in spin-glass transitions similar to those seen in other disordered RP phases (4, 18,19).

The temperature dependence of the resistivity is shown in Fig. 9. Plots of ln ρ vs $1/T$ are nonlinear with the high-temperature region activation energies given in Table 1. All these compounds are insulating with the $x = 1$ sample having the highest and the $x = 2$ phase having the lowest resistivity. These trends have been reported in other RP phases (18, 19, 25). The lower resistivity can be rationalized using similar arguments as these of MacChesney *et al.* (26). The larger iron concentration in the $x = 2$ phase requires a higher average oxidation state for the Fe ions. The overlap

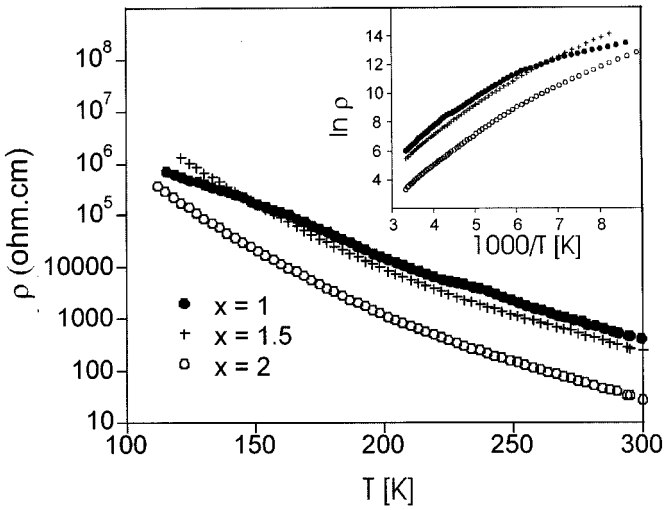

FIG. 9. Temperature-dependent resistivity data for $Sr_4Mn_{3-x}Fe_xO_{10-\delta}$. (Inset) ln ρ vs $1000/T$.

between the Fe t_{2g} and O p orbitals form a conduction band lowering the resistivity. If the oxygen content can be increased we predict that the resistivity would further drop due to better overlap.

CONCLUSIONS

We have prepared a series of iron-substituted $Sr_4Mn_{3-x}Fe_xO_{10}$ ($x = 1$, 3/2, and 2) compounds that form in the $n = 3$ RP structure. The Mn and Fe ions are randomly distributed; however, the Fe ions preferentially occupy the middle perovskite layer Mn/Fe(1), and this effectively stabilizes the RP, in contrast to the $Sr_4Mn_3O_{10}$ structure. The samples are oxygen deficient with both Fe^{3+} and possibly some Mn^{3+} present as evidenced by XANES. The $Sr_4Mn_2FeO_{9.72}$ sample orders antiferromagnetically around 90 K; all the samples studied here show spin-glass-like behavior at low temperature consistent with the random distribution of magnetic interactions. Mössbauer spectroscopy indicates that Fe^{4+} undergoes charge disproportionation ($2\,Fe^{4+} \rightarrow Fe^{3+\varepsilon} + Fe^{4+\delta}$), further complicating interpretation of the electronic and magnetic data.

ACKNOWLEDGMENTS

This work was supported by the NSF-Solid State Chemistry Grant DMR 96-13106. We thank Drs. J. Richardson and C. Murphy at the IPNS-Argonne National Laboratories for their help with the neutron data, and Professor W. H. McCarroll for his critical reading of the manuscript. G. Veith thanks the Department of Education for his GAANN fellowship.

REFERENCES

1. C. N. R. Rao, A. K. Cheetham, and R. Mahesh, *Chem. Mater.* **8,** 2421 (1996).

2. C. Zener, *Phys. Rev.* **82,** 403 (1951).
3. R. Gundakaram, A. Arulraj, P. V. Vanitha, C. N. R. Rao, N. Gayathri, A. K. Raychaudhuri, and A. K. Cheetham, *J. Solid State Chem.* **127,** 354 (1996).
4. P. D. Battle, W. R. Brandford, A. Mihut, M. J. Rosseinsky, J. Singleton, J. Sloan, L. E. Spring, and J. F. Vente, *Chem. Mater.* **11,** 674 (1999).
5. S. N. Ruddlesden and P. Popper, *Acta Crystallogr.* **11,** 54 (1958).
6. J. Fábry, J. Hybler, Z. Jirák, K. Jurek, K. Malý, M. Nevàva, and V. Petøék, *J. Solid State Chem.* **73,** 520 (1988).
7. R. D. Shannon and C. T. Prewitt, *Acta Crystallogr. Sect. B* **25,** 925 (1969); R. D. Shannon, *Acta Crystallogr. Sect. A* **32,** 751 (1976).
8. A. C. Larson and R. B. von Dreele, GSAS-Generalized Crystal Structure Analysis System, Los Alamos National Laboratory Report No. LA-UR-86-748, 1987.
9. F. Licci, G. Turilli, and P. Ferro, *J. Magn. Magn. Mater.* **164,** L268 (1996).
10. H. J. Rossell, P. Goodman, S. Bulcock, R. H. March, S. J. Kenedy, T. J. White, F. J. Lincoln, and K. S. Murray, *Aust. J. Chem.* **49,** 205 (1996).
11. N. Flores, M. Harvieu, G. van Tendeloo, C. Michel, A. Maignan, and B. Raveau, *Solid State Sci.* **2,** 1 (2000).
12. C. Brisi and P. Rolando, *Ann. Chim.* (*Rome*) **59,** 385 (1969).
13. J. Sloan, P. D. Battle, M. A. Green, M. J. Rosseinsky, and J. F. Vente, *J. Solid State Chem.* **138,** 135 (1998).
14. M. Croft, D. Sills, M. Greenblatt, C. Lee, S.-W. Cheong, K.V. Ramanujachary, and D. Tran, *Phys. Rev. B* **55,** 8726 (1997).
15. Q. Qian, T. A. Tyson, C.-C. Kao, M. Croft, S.-W. Cheong, and M. Greenblatt, *Phys. Rev. B*, submitted.
16. I. Elfimov, V. Anisimov, and G. Sawatzky, *Phys. Rev. Lett.* **82,** 4264 (1999).
17. J. Jung, K. Kim, D. Eom, T. Noh, E. Choi, J. Yu, Y. Kwon, and Y. Chung, *Phys. Rev. B* **55,** 15489 (1999).
18. I. D. Fawcett, G. M. Veith, M. Greenblatt, M. Croft, and I. Nowik, *Solid State Sci.*, in press.
19. G. M. Veith, I. D. Fawcett, M. Greenblatt, M. Croft, and I. Nowik, *J. Inorg. Mater.*, in press.
20. G. Jonker, *Physica* **20,** 1118 (1954).
21. E. Banks and N. Tasima, *J. Appl. Phys.* **41,** 1186 (1970).
22. K. Ahn, X. Wu, K. Liu, and C. Chen, *Phys. Rev. B* **54,** 15,299 (1996).
23. P. D. Battle, S. K. Bollen, and A. V. Powell, *J. Solid State Chem.* **99,** 267 (1992).
24. P. Adler, *J. Solid State Chem.* **130,** 129 (1997).
25. S. E. Dann, M. T. Weller, D. B. Currie, M. F. Thomas, and A. D. Al-Rawwas, *J. Mater. Chem.* **12,** 1231 (1993).
26. J. B. MacChesney, R. C. Sherwood, and J. F. Potter, *J. Chem. Physics* **43,** 1907 (1963).